NANO LETTERS

pubs.acs.org/NanoLett Letter

Ultrafast Thermal Shock Synthesis and Porosity Engineering of 3D Hierarchical Cu−Bi Nanofoam Electrodes for Highly Selective Electrochemical CO_2 Reduction

Songyuan Yang,△ Huaizhu Wang,△ Yan Xiong, Mengfei Zhu, Jingjie Sun, Minghang Jiang, Pengbo Zhang, Jie Wei, Yizhi Xing, Zuoxiu Tie, and Zhong Jin*

Cite This: *Nano Lett.* 2023, 23, 10140−10147 Read Online

ACCESS | Metrics & More | Article Recommendations | Supporting Information

ABSTRACT: Massive production of practical metal or alloy based electrocatalysts for electrocatalytic CO_2 reduction reaction is usually limited by energy-extensive consumption, poor reproducibility, and weak adhesion on electrode substrates. Herein, we report the ultrafast thermal shock synthesis and porosity engineering of free-standing Cu−Bi bimetallic nanofoam electrocatalysts with 3D hierarchical porous structure and easily adjustable compositions. During the thermal shock process, the rapid heating and cooling steps in several seconds result in strong interaction between metal nanopowders to form multiphase nanocrystallines with abundant grain boundaries and metastable CuBi intermetallic phase. The subsequent porosity engineering process via acid etching and electroreduction creates highly porous Cu−Bi structures that can increase electrochemically active surface area and facilitate mass/charge transfer. Among the Cu−Bi nanofoam electrodes with different Cu/Bi ratios, the Cu_4Bi nanofoam exhibited the highest formate selectivity with a Faradaic efficiency of 92.4% at −0.9 V (vs reversible hydrogen electrode) and demonstrated excellent operation stability.

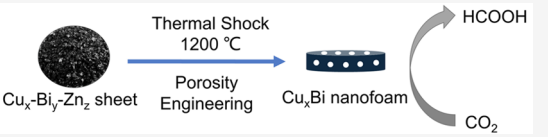

KEYWORDS: *Thermal shock synthesis, Porosity engineering, Free-standing metal/alloy nanofoam electrodes, 3D hierarchical porous nanostructures, Electrocatalytic CO_2-to-HCOOH conversion*

Electrochemical CO_2 reduction (CO_2RR) is a mild and controllable approach to realize carbon neturality and produce renewable energy.[1−6] However, the low activity of metal catalysts remains an obstacle for their practical application in CO_2RR due to high overpotential and low selectivity.[7−10] To overcome this challenge, researchers have been utilizing nanoengineering and alloying techniques to enhance the selectivity and activity of metal-based electrocatalysts.[11−14] Copper (Cu) is a common component in alloy owing to its excellent conductivity and intermediate adsorption behavior.[15] Additionally, bismuth (Bi) could suppress the hydrogen evolution reaction (HER) and exhibit an enhanced formate selectivity during the CO_2RR.[16] Notably, recent studies have reported Faradaic efficiencies approaching 100% for formate production using bismuth nanoflakes.[17] Besides, there are opportunities to enhance the overall performance and stability of Bi-based electrocatalysts for a broader range of applications through the formation of dual-metallic alloys, which benefits from the synergetic effects.[18] However, synthesizing these alloy materials often involves complex procedures to precisely adjust their nanostructure, which impede the reproducibility of large-scale production and result in excessive energy consumption.[19−21] Furthermore, many electrocatalysts have to be loaded onto electrode substrates such as carbon paper, glass carbon, and copper foam; the weak adhesion between the substrates and catalysts can result in detachment and instability.[22] Hence, it is crucial to prepare free-standing electrodes integrated with nanomanufacturing. Currently, scalable synthesis methods such as ultrafast high-temperature sintering and thermal shock have been developed to produce multiphase materials with enhanced mechanical properties.[23−25] These manufacturing techniques show promise for the fabrication of functional electrodes for the CO_2RR.

The 3D hierarchical Cu_xBi-NF electrodes were fabricated using commercially available Cu, Bi, and Zn powders through industrially feasible processes based on thermal shock treatment, acid etching, and subsequent electrochemical reduction (Figure 1a). Initially, various mole ratios of Cu, Bi, and Zn powders (Cu:Bi:Zn = 45:45:36, 60:30:36, 72:18:36, 80:10:36, 90:0:36, and 80:20:0) were blended through ball-milling and tableted to form $Cu_xBi_yZn_z$ sheets (namely $Cu_xBi_yZn_z$-MX, where x:y:z is the feeding mole ratio of Cu, Bi, and Zn powders, Supporting Information (SI), Figure S1a). The X-ray diffraction (XRD) patterns of these $Cu_xBi_yZn_z$-MX sheets were shown in SI, Figure S1b and S1c. Then, the $Cu_xBi_yZn_z$-MX samples were melted and solidified through

Received: June 27, 2023
Revised: October 31, 2023
Accepted: October 31, 2023
Published: November 6, 2023

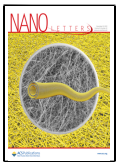

https://doi.org/10.1021/acs.nanolett.3c02380
Nano Lett. 2023, 23, 10140−10147

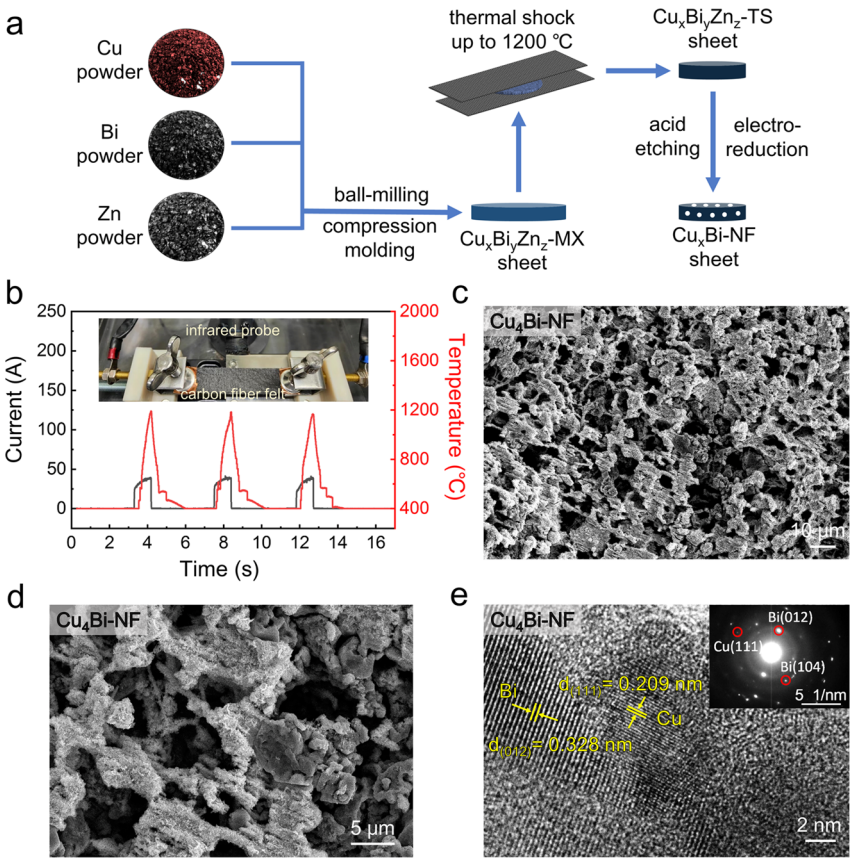

Figure 1. (a) Schematic illustration of the synthetic process of 3D hierarchical Cu_xBi-NF electrodes. (b) Time-dependent temperature and current plots during the thermal shock synthesis process of $Cu_xBi_yZn_z$-TS sheets. The inset shows an optical photograph of the homemade thermal shock instrument. (c,d) SEM and (e) HRTEM images of Cu_4Bi-NF.

thermal shock process in a homemade Joule heating instrument (the inset of Figure 1b), where carbon fiber felt acted as the thermal source. The thermal shock produced multiphase $Cu_xBi_yZn_z$ sheets (namely $Cu_xBi_yZn_z$-TS) were fabricated through three repeated rapid heating−cooling steps. The reaction temperature and time were carefully adjusted to facilitate the promotion of interphase reactions and prevent over melting of sheets. Three heating pulses ensured a relatively comprehensive reaction while minimizing the loss of components with lower melting points, resulting in a complete sheet with high mechanical strength. Figure 1b illustrates the time-dependent temperature and current profiles of the thermal shock process. The rapid heating step took only 0.6 s to raise the temperature to around 1200 °C and the cooling step took approximately 2.5 s. The XRD patterns of $Cu_xBi_yZn_z$-TS sheets are shown in SI, Figure S2a. Notably, the magnified XRD patterns (SI, Figure S2b) for $Cu_{80}Bi_{20}Zn_0$-TS sheets exhibit two weak peaks at around 30.3° and 32.7°, which are assigned to metastable CuBi intermetallic phase.[26] These two peaks do not exist in the XRD patterns of $Cu_xBi_yZn_z$-MX samples (SI, Figure S1c), indicating that the intermetallic phase is formed during the thermal shock process. The formation of the intermetallic phase certifies the strong interaction between the Cu and Bi species. Subsequently, the as-prepared $Cu_xBi_yZn_z$-TS sheets were etched in 1 M H_2SO_4 aqueous solution under ultrasonication and then electrochemically reduced in 0.1 M $KHCO_3$ aqueous solution to remove Zn and metal oxides species, as well as induce pores in the electrode. After the acid etching and electroreduction process, the final 3D hierarchical Cu_xBi-NF and Cu-NF electrodes are formed, where x is the simplified feeding mole ratio of Cu:Bi (e.g., the Cu_4Bi-NF was produced from $Cu_{72}Bi_{18}Zn_{36}$-TS and the Cu-NF was produced from $Cu_{90}Bi_0Zn_{36}$-TS). As a contrast sample without pore-engineering, the $Cu_{80}Bi_{20}Zn_0$ sheet was only electrochemically reduced without acid etching to form the reduced Cu_4Bi sheet (namely R-Cu_4Bi).

The morphological features of the samples were investigated by scanning electron microscopy (SEM). As shown in Figure 1c,d and SI, Figure S3, pore structures could be clearly observed in all the samples after porosity engineering. By comparing the SEM image of R-Cu_4Bi (SI, Figure S4a), $Cu_{72}Bi_{18}Zn_{36}$-TS (SI, Figure S4b, the precursor of Cu_4Bi-NF) and Cu_4Bi-NF (Figure 1c,d and SI, Figure S4c), it could be concluded that the quantity and hierarchy of pores obviously increased after etching. The uniform distributions of Cu and Bi species in Cu_4Bi-NF and R-Cu_4Bi are also proven by energy-dispersive X-ray spectroscopy (EDX) elemental mappings (SI, Figure S5).

The crystal phase characteristics of Cu_4Bi-NF were explored by high-resolution transmission electron microscopy (HRTEM), as shown in Figure 1e. The finger lattices of 0.328 and 0.209 nm are indexed to the Bi (012) and Cu (111) planes. The selective area electron diffraction (SAED) pattern of Cu_4Bi-NF (the inset in Figure 1e) exhibits several bright dots, which are assigned to the Bi (012), Bi (104), and Cu (111) planes, respectively. The grain boundary depicted in Figure 1e clearly confirms the copresence and perfect fusion of

https://doi.org/10.1021/acs.nanolett.3c02380
Nano Lett. 2023, 23, 10140−10147

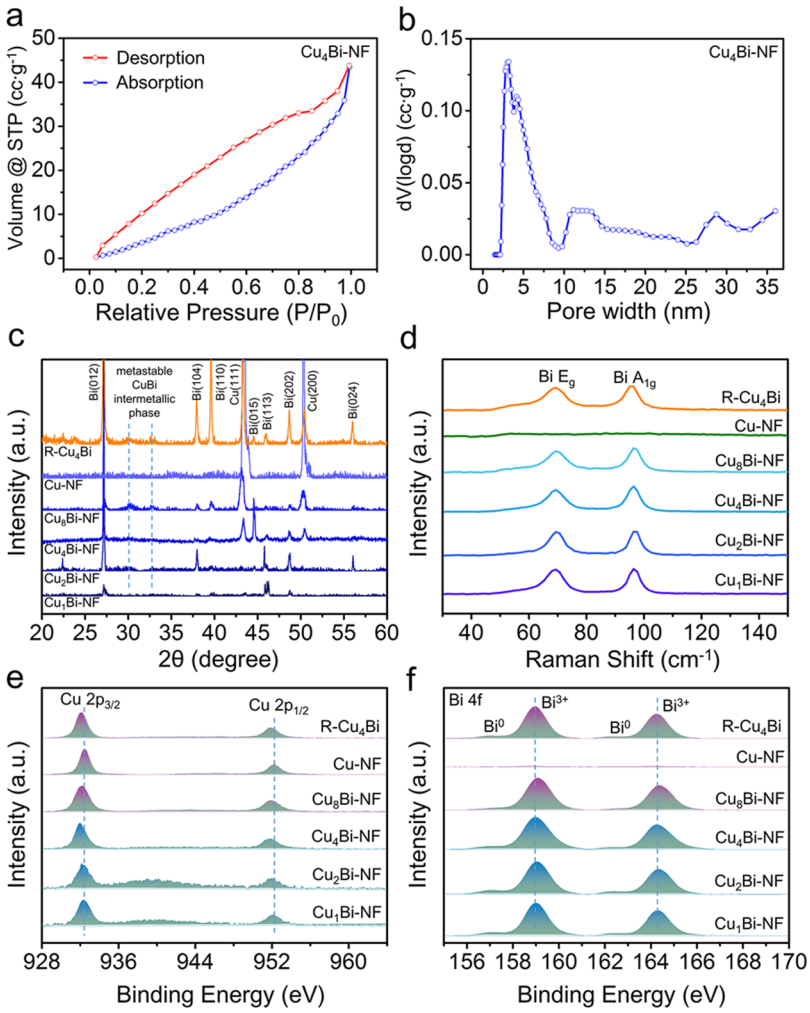

Figure 2. (a) N_2 absorption−desorption isotherms and (b) pore distribution of Cu_4Bi-NF. (c) XRD patterns, (d) Raman spectra, and (e,f) High-resolution XPS spectra at (e) Cu 2p and (f) Bi 4f regions of Cu_xBi-NF, Cu-NF, and R-Cu_4Bi samples.

Cu and Bi nanograins, which could potentially enhance electron transfer during electrochemical reactions.[27]

The porosity features of Cu_4Bi-NF and R-Cu_4Bi were investigated in detail via the Brunauer−Emmett−Teller (BET) method. N_2 adsorption−desorption isotherms revealed a specific large surface area of 74 $m^2 \cdot g^{-1}$ for Cu_4Bi-NF (Figure 2a). The total pore volume was calculated to be 6.723×10^{-2} $cc \cdot g^{-1}$, and the pore size distribution indicated the presence of mesopores and cavities mainly ranging from 2 to 35 nm (Figure 2b). In contrast, R-Cu_4Bi displayed a significantly lower surface area of 11 $m^2 \cdot g^{-1}$ and a total pore volume of 1.500×10^{-2} $cc \cdot g^{SI-1}$. Supporting Information, Figure S4e, illustrates that R-Cu_4Bi displays a distinctive stepped adsorption process, typical of a type VI adsorption isotherm.[28] This suggests that these steps may result from successive multilayer adsorption on a relatively smooth surface. Comparing SI, Figure S4f, to Figure 2b reveals that the porosity engineering process has enriched the Cu_4Bi-NF sample with a more diverse pore structure, resulting in a significant increase in pore capacity, size distribution, and overall catalyst-specific surface area enhancement. Based on the results of SEM and BET characterizations, it can be concluded that 3D hierarchical porous structure exist in the Cu_4Bi-NF, which could enhance the electrochemical reaction kinetics.[29]

According to the XRD patterns shown in Figure 2c, the Cu_xBi-NF and R-Cu_4Bi samples are composed of metallic Bi and metallic Cu, indicating that metal oxides are removed from these samples by electroreduction. No solid solution phase of Cu−Bi exists because Cu and Bi are mutually insoluble.[30] However, magnified XRD patterns (SI, Figure S6) show two weak peaks at 30.3° and 32.7° for Cu_2Bi-NF, Cu_4Bi-NF, Cu_8Bi-NF, and R-Cu_4Bi samples, suggesting that the metastable CuBi intermetallic phase produced by thermal shock process still remained. Raman spectra prove the existence of metallic Bi in the Cu_xBi-NF electrodes, as shown in Figure 2d. Two characteristic peaks of metallic Bi at 71 cm^{-1} (E_g mode) and 98 cm^{-1} (A_{1g} mode) can be clearly observed, and no signal of Bi^{3+} species can be found.[31] The elemental compositions and valence states of the samples were probed by X-ray photoelectron spectroscopy (XPS). All of the XPS results have been corrected according to the standard C 1s peak at 284.6 eV. The normalized Cu 2p XPS spectra (Figure 2e) show that the characteristic peaks correspond to either Cu^0 or Cu^+. Negative shifts of Cu binding energy could be clearly distinguished for the Cu_2Bi-NF, Cu_4Bi-NF, Cu_8Bi-NF, and R-Cu_4Bi when compared with the Cu-NF. These shifts indicate an electron transfer from Bi to Cu, which is conducive to promoting the synergistic effect.[32] The normalized Bi 4f XPS spectra (Figure 2f) could be fitted to

https://doi.org/10.1021/acs.nanolett.3c02380
Nano Lett. 2023, 23, 10140−10147

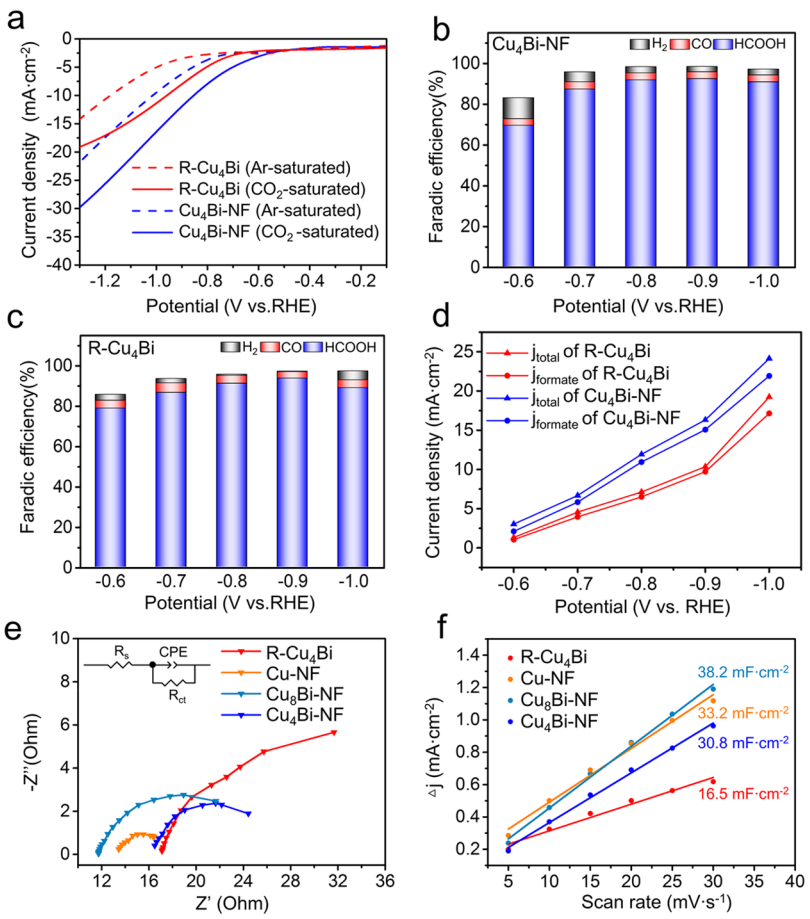

Figure 3. (a) LSV curves of Cu_4Bi-NF and R-Cu_4Bi measured in 0.1 M CO_2- or Ar-saturated $KHCO_3$ electrolyte, respectively. (b,c) Faradaic efficiencies of the reduction products generated by (b) Cu_4Bi-NF and (c) R-Cu_4Bi in 0.1 M CO_2-saturated $KHCO_3$ aqueous solution at different applied potentials. (d) Total current density (j_{total}) and partial current density for formate production ($j_{formate}$) of Cu_4Bi-NF and R-Cu_4Bi in 0.1 M CO_2 saturated $KHCO_3$ aqueous solution at different applied potentials. (e) Nyquist plots of Cu_4Bi-NF, Cu_8Bi-NF, Cu-NF, and R-Cu_4Bi samples in 0.1 M CO_2-saturated $KHCO_3$ solution at −0.9 V vs RHE. (f) Non-Faradaic charging current density differences (Δj) vs scan rates of Cu_4Bi-NF, Cu_8Bi-NF, Cu-NF, and R-Cu_4Bi samples.

two pairs of doublets associated with Bi^0 and Bi^{3+}. The XPS signals of Bi oxidation states in these samples were derived from surface oxidation of the catalyst due to exposure to air.

To verify the electrocatalytic activity of the samples, the linear sweep voltammetry (LSV) curves of these working electrodes were sequentially measured in 0.1 M Ar- and CO_2-saturated $KHCO_3$ electrolytes (Figure 3a, and SI, Figure S7a). In the CO_2-saturated electrolyte, a notably higher current density was observed for the Cu_4Bi-NF, Cu_8Bi-NF, R-Cu_4Bi, and $Cu_{72}Bi_{18}Zn_{36}$-TS within the potential window of −0.6 to −1.3 V vs RHE, indicating significant high CO_2RR catalytic activity of Bi species. As for the Cu-NF, the current density curve in the CO_2-saturated electrolyte is lower than that of the Ar-saturated electrolyte prior to −0.7 V and the current density remains similar after −0.7 V, indicating that there was no obvious enhancement for the Cu-NF to reduce CO_2. However, the current density of the Cu-NF reaches its maximum capacity earlier than other samples, demonstrating lowered impedance by Cu. Moreover, it was found that the Cu_4Bi-NF exhibited higher current densities compared to R-Cu_4Bi in both Ar- and CO_2-saturated electrolytes, indicating a decreased mass transfer resistance due to the pore structure.

The CO_2RR catalytic activities of the samples were measured in a 0.1 M CO_2-saturated $KHCO_3$ electrolyte solution using a two-compartment electrochemical cell separated by a Nafion-117 ion exchange membrane. The chronoamperometry curves at different working potentials are shown in SI, Figure S7b−S7h. The quantities of produced CO and H_2 gas were detected by gas chromatography (GC) and the quantity of produced formate was measured by anion chromatography. The calibration curve of $HCOO^-$ is presented in SI, Figure S8a. The Faradaic efficiencies for different electroreduction products at various applied potentials are detailed in Figure 3b,c and SI, Figure S8b−S8f. It is evident that all the samples containing Bi species exhibited a priority toward reducing CO_2 to HCOOH. The high selectivity toward formate could be attributed to the stabilization of *OCHO on Bi species, which ultimately transforms into HCOOH, as described by the following steps:[29]

$$CO_2(g) + {}^* + H^+(aq) + e^- \rightarrow {}^*OCHO \quad (1)$$

$$^*OCHO + H^+(aq) + e^- \rightarrow {}^*HCOOH \quad (2)$$

$$^*HCOOH \rightarrow HCOOH(aq) + {}^* \quad (3)$$

The $FE_{formate}$ of $Cu_{72}Bi_{18}Zn_{36}$-TS exhibits a slightly lower value compared to other Bi-containing samples due to the presence of competing reactions that produce CO. This is

https://doi.org/10.1021/acs.nanolett.3c02380
Nano Lett. 2023, 23, 10140−10147

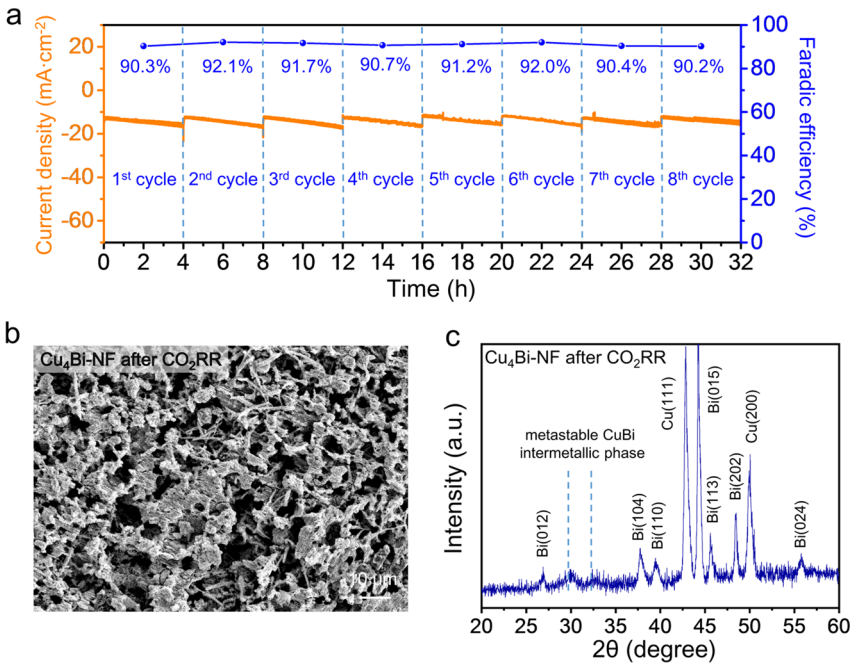

Figure 4. (a) Time-dependent current density and $FE_{Formate}$ of the Cu_4Bi-NF during long-term CO_2 electroreduction test for 32 h at an applied potential of −0.9 V vs RHE. (b) Corresponding SEM image and (c) XRD pattern of Cu_4Bi-NF after the long-term CO_2 electroreduction test for 32 h.

because Zn species tend to stabilize *COOH, which eventually transforms into CO, as shown in following:[33]

$$CO_2(g) + {}^* + H^+(aq) + e^- \rightarrow {}^*COOH \quad (4)$$

$${}^*COOH + H^+(aq) + e^- \rightarrow {}^*CO + H_2O(l) \quad (5)$$

$${}^*CO \rightarrow CO(g) + {}^* \quad (6)$$

On the other hand, the Cu-NF is not suitable for the CO_2RR because of the high FE_{H2} even though it exhibits a relatively high current density (SI, Figure S7a,S7f). This observation aligns with previous research findings, which have consistently indicated that Cu^0 exhibits lower proton reduction activity when compared to CuO_x and various copper alloys in the context of electrocatalytic CO_2 reduction.[34−37] The maximum $FE_{formate}$ for Cu_4Bi-NF and R-Cu_4Bi are 92.4% and 93.7% at −0.9 V vs RHE, which is significantly higher than Cu_1Bi-NF (86.1%), Cu_2Bi-NF (86.3%), Cu_8Bi-NF (86.8%), and $Cu_{72}Bi_{18}Zn_{36}$-TS (75.6%). Furthermore, it is observed that only the $FE_{formate}$ of the Cu_4Bi-NF and R-Cu_4Bi samples remained consistently high at over 85% within a wide potential range spanning from −0.7 to −1.0 V. Besides, the Cu_1Bi-NF and Cu_2Bi-NF were disintegrated into pieces after long-term CO_2RR tests, which indicated that they were not suitable for long-time applications due to the weak mechanical strength and integrity. Based on these findings, it could be concluded that the optimal feeding ratio of Cu to Bi is 4:1. The high selectivity of Cu_4Bi electrocatalysts for the electroreduction of CO_2 to formate could be ascribed to the synergetic effect between Cu and Bi nanograins and the metastable CuBi intermetallic phase. The observed enhancement in formic acid selectivity by the Cu−Bi catalysts can be attributed to several interconnected factors resulting from the interaction of copper and bismuth.[36,38,39] One of the foremost impacts of this interaction lies in its potential to significantly influence the electronic structure of the catalyst. Notably, because bismuth exhibits a higher electronegativity than copper,[40] this interaction serves to modulate the distribution of electron density within the catalyst, instigating a process of electronic restructuring, as discerned from the XPS results presented in Figure 2e,f. Such electron restructuring may yield stabilized reaction intermediates that favor the production of formic acid while concurrently depressing competing HER reaction or the formation of alternative carbon-based products.[41−43] Moreover, the interplay between copper and bismuth has been previously acknowledged for its potential to impact the nature and distribution of active sites on the surface of catalysts.[41,44,45] This effect can lead to the creation or modification of catalytic sites, improving reactivity and enhancing the affinity for CO_2 adsorption and conversion.

Additionally, due to the enhancement of mass transfer kinetics by the 3D hierarchical pore structure, which simultaneously accelerates both the CO_2RR and HER,[46] there is a slight decrease in $FE_{formate}$ for the Cu_4Bi-NF (92.4%) at −0.9 V vs RHE compared to the R-Cu_4Bi (93.7%), as a result of competition by the HER. Moreover, the total and partial current densities were calculated from chronoamperometry curves and $FE_{formate}$ for both Cu_4Bi-NF and R-Cu_4Bi (Figure 3d). The Cu_4Bi-NF exhibits the highest formate partial current density ($j_{formate}$) of 21.9 mA·cm^{-2} at −1.0 V (vs RHE), which is much higher than that of R-Cu_4Bi (17.1 mA·cm^{-2}), demonstrating successful depression of overpotential by the 3D porous structure. To facilitate further comparison, we have assembled the CO_2-to-HCOOH conversion performance data from other Bi-based and bimetallic electrocatalysts previously reported (SI, Table S1). This compilation underscores the competitive activity and selectivity of Cu_4Bi-NF catalysts, as demonstrated in this work, for the reduction of CO_2 in HCOOH production.

To further clarify the origin of CO_2RR performance differences for these samples, the electrochemical impedance spectra (EIS) of Cu_4Bi-NF, Cu_8Bi-NF, Cu-NF, and R-Cu_4Bi

https://doi.org/10.1021/acs.nanolett.3c02380
Nano Lett. 2023, 23, 10140−10147

samples were tested in 0.1 M CO_2-saturated $KHCO_3$ solution at −0.9 V vs RHE (Figure 3e). The Nyquist curves can be fitted by the equivalent circuit (see the inset of Figure 3e). The Cu_4Bi-NF exhibited an equivalent series resistance (R_{ct}) of 9.1 Ω, which is obviously smaller than that of Cu_8Bi-NF (12.0 Ω) and R-Cu_4Bi (21.2 Ω), illustrating the faster catalytic kinetics of Cu_4Bi-NF. The Cu-NF exhibited the lowest R_{ct} of only 3.9 Ω, indicating that charge transfer impedance could be highly decreased by Cu metal, which is identical to the results of LSV. Moreover, the CV curves at different scan rates were compared (SI, Figure S9). The double-layer capacitance (C_{dl}) values of Cu_4Bi-NF (30.8 mF·cm^{-2}), Cu_8Bi-NF (38.2 mF·cm^{-2}), Cu-NF (33.2 mF·cm^{-2}), and R-Cu_4Bi (16.5 mF·cm^{-2}) were calculated by linearly plotting the corresponding charging current density differences against the scan rates at the open-circuit potential, ensuring the non-Faradaic process. The above C_{dl} values suggest that the Cu_xBi-NF and Cu-NF samples possess a greater electrochemically active surface area (ECSA) than the R-Cu_4Bi because the ECSA is proportional to the C_{dl}. These electrochemical analysis results illustrate that the 3D hierarchical pore structure could greatly increase the number of effective active sites and accelerate the mass transfer process during the CO_2RR.

The electrocatalytic stability of Cu_4Bi-NF was evaluated by a long-term CO_2RR test in 0.1 M CO_2-saturated $KHCO_3$ electrolyte for 32 h (Figure 4a). The $FE_{formate}$ for liquid products were analyzed between the cycles of 4 h. The $FE_{formate}$ remained above 90% throughout 8 cycles with no significant attenuation in current densities. The surface morphology of Cu_4Bi-NF after long-term CO_2RR test was investigated by SEM (Figure 4b), which revealed that the pore structure was well maintained. Furthermore, the main peaks in XRD patterns (Figure 4c) are identical with those before the CO_2RR test (Figure 2c). Only a weak decrease of Bi (012) intensity and a slight increase of Bi (015) intensity were observed, which might be caused by the crystal phase transition during the CO_2RR. The metastable CuBi intermetallic phase still can be clearly distinguished, indicating stable interaction between Cu and Bi. These results confirm that Cu_4Bi-NF exhibits excellent electrocatalytic durability and structural stability for the CO_2RR.

In summary, we report a rapid and controllable strategy for the fabrication of a series of free-standing 3D hierarchical Cu−Bi nanofoam electrodes through thermal shock synthesis and porosity engineering toward highly selective electrochemical reduction of CO_2 to HCOOH. Among these samples, the Cu_4Bi-NF exhibits the best electrocatalytic performances owing to the synergetic effect between Cu and Bi, which efficiently decreases charge transfer impedance. Additionally, the Cu_4Bi-NF has a larger ECSA than R-Cu_4Bi sheet, which decreases the overpotential for CO_2RR toward HCOOH product due to the mass transfer kinetics enhanced by 3D porous structure. The Cu_4Bi-NF electrode also demonstrates excellent long-term catalytic durability. These findings offer a robust pathway to efficiently produce scalable metal-/alloy-based free-standing 3D hierarchical porous nanofoam electrodes, which can also be broadly extended to other domains within clean electrochemical energy conversion.

■ ASSOCIATED CONTENT

Supporting Information

The Supporting Information is available free of charge at https://pubs.acs.org/doi/10.1021/acs.nanolett.3c02380.

Experimental methods, figures showing additional characterization and electrochemical activity data, and table showing performance comparisons (PDF)

■ AUTHOR INFORMATION

Corresponding Author

Zhong Jin − *State Key Laboratory of Coordination Chemistry, MOE Key Laboratory of Mesoscopic Chemistry, MOE Key Laboratory of High Performance Polymer Materials and Technology, Jiangsu Key Laboratory of Advanced Organic Materials, School of Chemistry and Chemical Engineering, Nanjing University, Nanjing, Jiangsu 210023, P. R. China;* orcid.org/0000-0001-8860-8579; Email: zhongjin@nju.edu.cn

Authors

Songyuan Yang − *State Key Laboratory of Coordination Chemistry, MOE Key Laboratory of Mesoscopic Chemistry, MOE Key Laboratory of High Performance Polymer Materials and Technology, Jiangsu Key Laboratory of Advanced Organic Materials, School of Chemistry and Chemical Engineering, Nanjing University, Nanjing, Jiangsu 210023, P. R. China*

Huaizhu Wang − *State Key Laboratory of Coordination Chemistry, MOE Key Laboratory of Mesoscopic Chemistry, MOE Key Laboratory of High Performance Polymer Materials and Technology, Jiangsu Key Laboratory of Advanced Organic Materials, School of Chemistry and Chemical Engineering, Nanjing University, Nanjing, Jiangsu 210023, P. R. China*

Yan Xiong − *State Key Laboratory of Coordination Chemistry, MOE Key Laboratory of Mesoscopic Chemistry, MOE Key Laboratory of High Performance Polymer Materials and Technology, Jiangsu Key Laboratory of Advanced Organic Materials, School of Chemistry and Chemical Engineering, Nanjing University, Nanjing, Jiangsu 210023, P. R. China*

Mengfei Zhu − *State Key Laboratory of Coordination Chemistry, MOE Key Laboratory of Mesoscopic Chemistry, MOE Key Laboratory of High Performance Polymer Materials and Technology, Jiangsu Key Laboratory of Advanced Organic Materials, School of Chemistry and Chemical Engineering, Nanjing University, Nanjing, Jiangsu 210023, P. R. China*

Jingjie Sun − *State Key Laboratory of Coordination Chemistry, MOE Key Laboratory of Mesoscopic Chemistry, MOE Key Laboratory of High Performance Polymer Materials and Technology, Jiangsu Key Laboratory of Advanced Organic Materials, School of Chemistry and Chemical Engineering, Nanjing University, Nanjing, Jiangsu 210023, P. R. China*

Minghang Jiang − *State Key Laboratory of Coordination Chemistry, MOE Key Laboratory of Mesoscopic Chemistry, MOE Key Laboratory of High Performance Polymer Materials and Technology, Jiangsu Key Laboratory of Advanced Organic Materials, School of Chemistry and Chemical Engineering, Nanjing University, Nanjing, Jiangsu 210023, P. R. China; Department of Chemistry, School of Science, Xihua University, Chengdu, Sichuan 610039, P. R. China*

Pengbo Zhang − *State Key Laboratory of Coordination Chemistry, MOE Key Laboratory of Mesoscopic Chemistry, MOE Key Laboratory of High Performance Polymer Materials and Technology, Jiangsu Key Laboratory of*

https://doi.org/10.1021/acs.nanolett.3c02380
Nano Lett. 2023, 23, 10140−10147

Advanced Organic Materials, School of Chemistry and Chemical Engineering, Nanjing University, Nanjing, Jiangsu 210023, P. R. China

Jie Wei − *State Key Laboratory of Coordination Chemistry, MOE Key Laboratory of Mesoscopic Chemistry, MOE Key Laboratory of High Performance Polymer Materials and Technology, Jiangsu Key Laboratory of Advanced Organic Materials, School of Chemistry and Chemical Engineering, Nanjing University, Nanjing, Jiangsu 210023, P. R. China*

Yizhi Xing − *State Key Laboratory of Coordination Chemistry, MOE Key Laboratory of Mesoscopic Chemistry, MOE Key Laboratory of High Performance Polymer Materials and Technology, Jiangsu Key Laboratory of Advanced Organic Materials, School of Chemistry and Chemical Engineering, Nanjing University, Nanjing, Jiangsu 210023, P. R. China*

Zuoxiu Tie − *State Key Laboratory of Coordination Chemistry, MOE Key Laboratory of Mesoscopic Chemistry, MOE Key Laboratory of High Performance Polymer Materials and Technology, Jiangsu Key Laboratory of Advanced Organic Materials, School of Chemistry and Chemical Engineering, Nanjing University, Nanjing, Jiangsu 210023, P. R. China; Jiangsu BTR Nano Technology Co., Ltd., Changzhou, Jiangsu 213200, P. R. China; Nanjing Tieming Energy Technology Co. Ltd., Nanjing, Jiangsu 210093, P. R. China; Suzhou Tierui New Energy Technology Co. Ltd., Suzhou, Jiangsu 215228, P. R. China*

Complete contact information is available at: https://pubs.acs.org/10.1021/acs.nanolett.3c02380

Author Contributions

△S.Y.Y. and H.Z.W. contributed equally to this work. Z.J. conceived the idea of this study. S.Y.Y. and H.Z.W. designed the experiments. S.Y.Y., H.Z.W., Y.Z.X. and M.H.J. performed the sample fabrication, electrochemical measurements, and data analysis. S.Y.Y., M.F.Z., J.J.S., J.W., P.B.Z. and Z.X.T. performed the material characterizations. S.Y.Y., H.Z.W., Y.X. and Z.J. wrote and revised the paper. Z.J. planned and supervised the project.

Notes

The authors declare no competing financial interest.

■ ACKNOWLEDGMENTS

We appreciate the financial support from the National Natural Science Foundation of China (no. 22022505), the Fundamental Research Funds for the Central Universities of China (nos. 020514380266, 020514380272, and 020514380274), the Scientific and Technological Innovation Special Fund for Carbon Peak and Carbon Neutrality of Jiangsu Province (no. BK20220008), the Scientific and Technological Achievements Transformation Special Fund of Jiangsu Province (no. BA2023037), the International Collaboration Research Program of Nanjing City (nos. 202201007 and 2022SX00000955), and the Gusu Leading Talent Program of Scientific and Technological Innovation and Entrepreneurship of Wujiang District in Suzhou City (no. ZXL2021273).

■ REFERENCES

(1) Tian, J. F.; Yu, L. G.; Xue, R.; Zhuang, S.; Shan, Y. L. Global Low-carbon Energy Transition in the Post-COVID-19 Era. *Appl. Energy* **2022**, *307*, 118205.

(2) Lamb, W. F.; Wiedmann, T.; Pongratz, J.; Andrew, R.; Crippa, M.; Olivier, J. G. J.; Wiedenhofer, D.; Mattioli, G.; Al Khourdajie, A.; House, J.; et al. A Review of Trends and Drivers of Greenhouse Gas Emissions by Sector from 1990 to 2018. *Environ. Res. Lett.* **2021**, *16* (7), No. 073005.

(3) Saravanan, A.; Senthil kumar, P.; Vo, D.-V. N.; Jeevanantham, S.; Bhuvaneswari, V.; Anantha Narayanan, V.; Yaashikaa, P.R.; Swetha, S.; Reshma, B. A Comprehensive Review on Different Approaches for CO_2 Utilization and Conversion Pathways. *Chem. Eng. Sci.* **2021**, *236*, 116515.

(4) Han, N.; Ding, P.; He, L.; Li, Y. Y.; Li, Y. G. Promises of Main Group Metal-Based Nanostructured Materials for Electrochemical CO_2 Reduction to Formate. *Adv. Energy Mater.* **2020**, *10*, 1902338.

(5) Francke, R.; Schille, B.; Roemelt, M. Homogeneously Catalyzed Electroreduction of Carbon Dioxide-Methods, Mechanisms, and Catalysts. *Chem. Rev.* **2018**, *118* (9), 4631−4701.

(6) Birdja, Y. Y.; Perez-Gallent, E.; Figueiredo, M. C.; Gottle, A. J.; Calle-Vallejo, F.; Koper, M. T. M. Advances and Challenges in Understanding the Electrocatalytic Conversion of Carbon Dioxide to Fuels. *Nat. Energy* **2019**, *4* (9), 732−745.

(7) Franco, F.; Rettenmaier, C.; Jeon, H. S.; Roldan Cuenya, B. Transition Metal-based Catalysts for the Electrochemical CO_2 Reduction: from Atoms and Molecules to Nanostructured Materials. *Chem. Soc. Rev.* **2020**, *49* (19), 6884−6946.

(8) Thijs, B.; Ronge, J.; Martens, J. A. Matching Emerging Formic Acid Synthesis Processes with Application Requirements. *Green Chem.* **2022**, *24* (6), 2287−2295.

(9) Chen, C.; Khosrowabadi Kotyk, J. F.; Sheehan, S. W. Progress toward Commercial Application of Electrochemical Carbon Dioxide Reduction. *Chem* **2018**, *4*, 2571−2586.

(10) Jin, S.; Hao, Z. M.; Zhang, K.; Yan, Z. H.; Chen, J. Advances and Challenges for the Electrochemical Reduction of CO_2 to CO: From Fundamentals to Industrialization. *Angew. Chem., Int. Ed.* **2021**, *60* (38), 20627−20648.

(11) Hsieh, Y. C.; Senanayake, S. D.; Zhang, Y.; Xu, W. Q.; Polyansky, D. E. Effect of Chloride Anions on the Synthesis and Enhanced Catalytic Activity of Silver Nanocoral Electrodes for CO_2 Electroreduction. *ACS Catal.* **2015**, *5* (9), 5349−5356.

(12) Zhu, W. J.; Zhang, L.; Yang, P. P.; Hu, C. L.; Luo, Z. B.; Chang, X. X.; Zhao, Z. J.; Gong, J. L. Low-Coordinated Edge Sites on Ultrathin Palladium Nanosheets Boost Carbon Dioxide Electroreduction Performance. *Angew. Chem., Int. Ed.* **2018**, *57* (36), 11544−11548.

(13) Zhang, W. J.; Hu, Y.; Ma, L. B.; Zhu, G. Y.; Wang, Y. R.; Xue, X. L.; Chen, R. P.; Yang, S. Y.; Jin, Z. Progress and Perspective of Electrocatalytic CO_2 Reduction for Renewable Carbonaceous Fuels and Chemicals. *Adv. Sci.* **2018**, *5*, 1700275.

(14) He, J. F.; Johnson, N. J. J.; Huang, A. X.; Berlinguette, C. P. Electrocatalytic Alloys for CO_2 Reduction. *ChemSusChem* **2018**, *11* (1), 48−57.

(15) Vasileff, A.; Xu, C. C.; Jiao, Y.; Zheng, Y.; Qiao, S. Z. Surface and Interface Engineering in Copper-Based Bimetallic Materials for Selective CO_2 Electroreduction. *Chem.* **2018**, *4* (8), 1809−1831.

(16) Guan, Y. Y.; Liu, M. M.; Rao, X. F.; Liu, Y. Y.; Zhang, J. J. Electrochemical Reduction of Carbon Dioxide (CO_2): Bismuth-based Electrocatalysts. *J. Mater. Chem. A* **2021**, *9* (24), 13770−13803.

(17) Kim, S.; Dong, W. J.; Gim, S.; Sohn, W.; Park, J. Y.; Yoo, C. J.; Jang, H. W.; Lee, J. L. Shape-Controlled Bismuth Nanoflakes as Highly Selective Catalysts for Electrochemical Carbon Dioxide Reduction to Formate. *Nano Energy* **2017**, *39*, 44−52.

(18) Chen, W.; Wang, Y.; Li, Y.; Li, C. Electrocatalytic CO_2 Reduction over Bimetallic Bi-Based Catalysts: A Review. *CCS Chem.* **2023**, *5* (3), 544−567.

(19) An, C.; Shen, Y. L.; Yan, W. X.; Dai, L. X.; An, C. H. Surface-tuning Nanoporous $AuCu_3$ Engineering Syngas Proportion by Electrochemical Conversion of CO_2. *Nano Res.* **2021**, *14* (11), 3907−3912.

(20) Lv, H.; Lv, F.; Qin, H.; et al. Single-crystalline Mesoporous Palladium and Palladium-Copper Nanocubes for Highly Efficient Electrochemical CO_2 Reduction. *CCS Chem.* **2022**, *4* (4), 1376−1385.

(21) She, X.; Wang, Y.; Xu, H.; Chi Edman Tsang, S.; Ping Lau, S. Challenges and Opportunities in Electrocatalytic CO_2 Reduction to Chemicals and Fuels. *Angew. Chem., Int. Ed.* **2022**, *61* (49), No. e202211396.
(22) Yang, H. P.; Wang, X. D.; Hu, Q.; Chai, X. Y.; Ren, X. Z.; Zhang, Q. L.; Liu, J. H.; He, C. X. Recent Progress in Self-Supported Catalysts for CO_2 Electrochemical Reduction. *Small Methods* **2020**, *4*, 1900826.
(23) Shibuya, Y.; Zhang, J. W.; Sato, Y.; Yanagimoto, J. Enhancement of Mechanical Property and Formability of CFRP Core Sandwich Sheets by Additive Manufacturing Process-induced Material and Structural Anisotropies. *J. Mater. Process. Technol.* **2022**, *310*, 117778.
(24) Wang, C. W.; Ping, W. W.; Bai, Q.; Cui, H. C.; Hensleigh, R.; Wang, R. L.; Brozena, A. H.; Xu, Z. P.; Dai, J. Q.; Pei, Y.; et al. A General Method to Synthesize and Sinter Bulk Ceramics in Seconds. *Science* **2020**, *368* (6490), 521−526.
(25) Liu, S. L.; Hu, Z.; Wu, Y. Z.; Zhang, J. F.; Zhang, Y.; Cui, B. H.; Liu, C.; Hu, S.; Zhao, N. Q.; Han, X. P.; et al. Dislocation-Strained IrNi Alloy Nanoparticles Driven by Thermal Shock for the Hydrogen Evolution Reaction. *Adv. Mater.* **2020**, *32*, 2006034.
(26) Hoffman, Z. B.; Gray, T. S.; Xu, Y.; Lin, Q. Y.; Gunnoe, T. B.; Zangari, G. High Selectivity Towards Formate Production by Electrochemical Reduction of Carbon Dioxide at Copper-Bismuth Dendrites. *ChemSusChem* **2019**, *12* (1), 231−239.
(27) Li, H. X.; Yue, X.; Che, J.; Xiao, Z.; Yu, X. B.; Sun, F. L.; Xue, C.; Xiang, J. H. High Performance 3D Self-Supporting Cu-Bi Aerogels for Electrocatalytic Reduction of CO_2 to Formate. *ChemSusChem* **2022**, *15*, No. e202200226.
(28) Rouquerol, F.; Rouquerol, J.; Sing, K. S. W. *Adsorption by Powders and Porous Solids: Principles, Methodology, and Applications*, 2nd ed.; Academic Press: Kidlington, Oxford, 2014.
(29) Zhang, W. J.; Yang, S. Y.; Jiang, M. H.; Hu, Y.; Hu, C. Q.; Zhang, X. L.; Jin, Z. Nanocapillarity and Nanoconfinement Effects of Pipet-like Bismuth@Carbon Nanotubes for Highly Efficient Electrocatalytic CO_2 Reduction. *Nano Lett.* **2021**, *21* (6), 2650−2657.
(30) Chakrabarti, D. J.; Laughlin, D. E. The Bi-Cu (bismuth-copper) system. *Bull. Alloy Phase Diagrams* **1984**, *5* (2), 148−155.
(31) Deng, P. L.; Wang, H. M.; Qi, R. J.; Zhu, J. X.; Chen, S. H.; Yang, F.; Zhou, L.; Qi, K.; Liu, H. F.; Xia, B. Y. Bismuth Oxides with Enhanced Bismuth-Oxygen Structure for Efficient Electrochemical Reduction of Carbon Dioxide to Formate. *ACS Catal.* **2020**, *10* (1), 743−750.
(32) Zhang, Z. R.; Liu, W. H.; Zhang, W.; Liu, M. M.; Huo, S. J. Interface Interaction in CuBi Catalysts with Tunable Product Selectivity for Electrochemical CO_2 Reduction Reaction. *Colloid. Surface A* **2021**, *631*, 127637.
(33) Xiao, J.; Gao, M. R.; Liu, S. B.; Luo, J. L. Hexagonal Zn Nanoplates Enclosed by Zn(100) and Zn(002) Facets for Highly Selective CO_2 Electroreduction to CO. *ACS Appl. Mater. Interfaces* **2020**, *12* (28), 31431−31438.
(34) Merino-Garcia, I.; Albo, J.; Krzywda, P.; Mul, G.; Irabien, A. Bimetallic Cu-Based Hollow Fibre Electrodes for CO_2 Electroreduction. *Catal. Today* **2020**, *346*, 34−39.
(35) Albo, J.; Irabien, A. Cu_2O-Loaded Gas Diffusion Electrodes for the Continuous Electrochemical Reduction of CO_2 to Methanol. *J. Catal.* **2016**, *343*, 232−239.
(36) Nitopi, S.; Bertheussen, E.; Scott, S. B.; Liu, X.; Engstfeld, A. K.; Horch, S.; Seger, B.; Stephens, I. E. L.; Chan, K.; Hahn, C.; Nørskov, J. K.; Jaramillo, T. F.; Chorkendorff, I. Progress and Perspectives of Electrochemical CO_2 Reduction on Copper in Aqueous Electrolyte. *Chem. Rev.* **2019**, *119*, 7610−7672.
(37) Albo, J.; Sáez, A.; Solla-Gullón, J.; Montiel, V.; Irabien, A. Production of Methanol from CO_2 Electroreduction at Cu_2O and Cu_2O/ZnO-Based Electrodes in Aqueous Solution. *Appl. Catal., B* **2015**, *176*−*177*, 709−717.
(38) Merino-Garcia, I.; Albo, J.; Krzywda, P.; Mul, G.; Irabien, A. Bimetallic Cu-Based Hollow Fiber Electrodes for CO_2 Electroreduction. *Cata. Today* **2020**, *346*, 34−39.
(39) Perfecto-Irigaray, M.; Albo, J.; Beobide, G.; Castillo, O.; Irabien, A.; Pérez-Yáñez, S. Synthesis of Heterometallic Metal-Organic Frameworks and Their Performance as Electrocatalyst for CO_2 Reduction. *RSC Adv.* **2018**, *8* (38), 21092−21099.
(40) Tantardini, C.; Oganov, A. R. Thermochemical electronegativities of the elements. *Nat. Commun.* **2021**, *12*, 2087.
(41) Zhu, Y.; Cui, X.; Liu, H.; Guo, Z.; Dang, Y.; Fan, Z.; Zhang, Z.; Hu, W. Tandem catalysis in electrochemical CO_2 reduction reaction. *Nano Res.* **2021**, *14*, 4471−4486.
(42) Albo, J.; Beobide, G.; Castaño, P.; Irabien, A. Methanol Electrosynthesis from CO_2 at Cu_2O/ZnO Prompted by Pyridine-Based Aqueous Solutions. *J. CO2 Util.* **2017**, *18*, 164−172.
(43) Merino-Garcia, I.; Albo, J.; Solla-Gullón, J.; Montiel, V.; Irabien, A. Cu Oxide/ZnO-Based Surfaces for a Selective Ethylene Production from Gas-Phase CO_2 Electroconversion. *J. CO2 Util.* **2019**, *31*, 135−142.
(44) Albo, J.; Perfecto-Irigaray, M.; Beobide, G.; Irabien, A. Cu/Bi Metal-Organic Framework-Based Systems for an Enhanced Electrochemical Transformation of CO_2 to Alcohols. *J. CO2 Util.* **2019**, *33*, 157−165.
(45) Albo, J.; Vallejo, D.; Beobide, G.; Castillo, O.; Castaño, P.; Irabien, A. Copper-Based Metal-Organic Porous Materials for CO_2 Electrocatalytic Reduction to Alcohols. *ChemSusChem* **2017**, *10* (6), 1100−1109.
(46) Li, M. R.; Idros, M. N.; Wu, Y. M.; Burdyny, T.; Garg, S.; Zhao, X. S.; Wang, G.; Rufford, T. E. The Role of Electrode Wettability in Electrochemical Reduction of Carbon Dioxide. *J. Mater. Chem. A* **2021**, *9* (35), 19369−19409.

https://doi.org/10.1021/acs.nanolett.3c02380
Nano Lett. 2023, 23, 10140−10147